Performance of nano titania-reinforced slag/basalt geopolymer composites

Hani A. Mashout[1], Taha A. Razek[1], Mohamed S. Amin[2,3], Fayza S. Hashem[2*] and Faten A. Selim[2]

*Correspondence:
f_s_hashem@ymail.com

[1] Faculty for Environmental Studies and Research, Ain Shams University, Cairo, Egypt
[2] Chemistry Department, Faculty of Science, Ain Shams University, Cairo, Egypt
[3] Chemistry Department, College of Science, Taibah University, Al-Madinah Al-Munawarah, Saudi Arabia

Abstract

In Egypt, basalt manufacturing generates waste materials at a rate of about 33%. The disposal of basalt waste through the manufacturing of cementitious materials is an economically feasible approach. This work involved the fabrication of a one-part slag/basalt waste geopolymer cement (GP) enhanced by nano-TiO$_2$. The physico-mechanical properties of the different GP mixes were investigated. The durability against fire at up to 750 °C, sulfate (SO$_4^{-2}$) attack, and irradiation with significant dosages of γ-rays at up to 1500 kGy were assessed. Phase composition and microstructure were explored through various techniques as XRD, TG, and SEM. The findings demonstrated that basalt incorporation up to 20% within the GP mix boosted its mechanical characteristics after 28 and 90 days of curing by 8.5 and 2.5%, respectively, while 60% replacement diminished the strength by 30%. Slag/basalt GP showed a comprehensible resistance to SO$_4^{-2}$ ions attack, and its strength was intensified by 14% after 4 months of immersion. Additionally, the blended GP mixes could preserve 40% of their strength after being exposed to 1500 kGy of γ-rays and about 50% of their strength after firing at 750 °C. Admixing GP by NT showed a synergic impact for diminishing setting times, boosting compressive strength by 5 ~ 15% compared to reference mix along with an improvement in the microstructure. Furthermore, distributing NT through GP greatly improved durability after firing at 500 and 700 °C and irradiating with high dosages of γ-rays. This feature is mostly connected to the catalytic capabilities and filling activities of NT in boosting geopolymerization processes.

Keywords: Compressive strength, Durability, Gamma irradiation, Nano-TiO$_2$, One-mix geopolymer

Introduction

There is a significant demand for high-performance and more sustainable construction materials due to the continued economic expansion in the world. One of the most significant building materials used worldwide is Portland cement (PC). Nevertheless, owing to the burning of carbonaceous materials and fuel consumption, manufacturing of PC has run into several environmental issues [1, 2]. Additionally, the PC production produces thousands of tons of hazardous emissions, including nitrogen oxides, dust, greenhouse gases, and sulfur dioxide [3, 4]. Scientists have been developing novel ecological and eco-friendly binders to replace Portland cement partially or completely in concrete mixtures [5, 6].

Mashout *et al. Journal of Engineering and Applied Science*   (2023) 70:106

Page 2 of 24

Alkali-activated cement or geopolymer cement (GP) is attracting an extra attention as an excellent binder that can replace PC in the building mix. Geopolymers (GPs) are cementitious composites that are free of PC [7]. Their production depends on the chemical treatment of aluminosilicate raw materials by alkaline activator through chemical reactions or polycondensation process that results in solidifying products of cementitious properties. The manufacture of geopolymer binders does not require limestone firing, which minimizes CO2 emissions in the surrounding environment [8]. Furthermore, industrial solid wastes can be used as primary supplies of alumina and silica in PC manufacture to reduce future accumulating problems [9–16]. There are several technical benefits of employing geopolymer as construction binders, including appropriate mechanical characteristics [17] and its better endurance in both acidic and corrosive ionic environments [18, 19]. Furthermore, those cement binders outperformed OPC in firing actions [20, 21]. Recently, geopolymer binders have found numerous outstanding incorporates in restoration supplies [22], structure composites [23], and pavement constructions [24].

There are two primary forms of geopolymer, as described in the literature, contingent on how GP is prepared or handled. The first type, known as the traditional or two-part geopolymer, is created when solid aluminosilicate precursors and concentrated solution of alkaline activator are combined [25, 26]. Nevertheless, there are several hazardous challenges with handling the concentrated alkali activator solution, which are reflected in the expand use of GP created using this method. The second type of geopolymer, known as one part or ready mix, is made by simply adding water to a mixture of an aluminum–silicate source and a dry alkaline activator as a one mix [9, 10, 27].

Basalt is an igneous rock that originates when lava cools on the surface of the Earth [28]. Basalt rock has a high silica content beside alumina, iron, and magnesium oxides. These minerals are present in an active state and change to a more amorphous state when the hot lava cools [29, 30]. Basalt stone can be used as a filter stone in drainage projects, while the crushed basalt is used to create the foundation for roads and pavements. There are two main basalt resources in South Egypt. About 240,000 m^3 of basalt aggregates and roughly 80,000 m^3 of fine-grained basalt residue are produced each year as a result of the crushing process. So about 33% of the basalt total production is produced as a waste material [31]. Basalt waste (BW) can be viewed as a natural pozzolana due to its characteristics as supplemental cementitious material (SCM) to OPC that have been widely researched [32, 33]. Numerous studies have recently attempted to use BW in the manufacture of alkali-activated binders or geopolymer composite [34–36]. However, a crucial factor for extending the use of basalt-based GP is its resistance to various degradation acts, which calls for more research.

A prevalent technique to promote a denser packing, lessen the tendency for cracks, and improve the compactness of the granular structure is the use of micro- and nanoparticles in cementitious materials. Examples of these materials with microscopic reinforcing activities are nano titania (NT), nano alumina (NA), silica (NS), carbon fibers (CF), and nano clays (NC) [37, 38]. NT has a wide range of uses, including the manufacture of photovoltaic solar cells [39, 40] and the photocatalytic destruction of contaminants in wastewater [41]. When micro- and nanoparticles are included into the geopolymer matrix, they can increase their effective volume within

Mashout *et al. Journal of Engineering and Applied Science*   (2023) 70:106

Page 3 of 24

the first hour of reaction and densify the matrix, creating a building structure with greater strength and better durability.

Few investigations have been conducted so far on the durability performance of one-part geopolymers made from basalt waste. The objective of this study is to determine how high temperatures, sulfate attack, and gamma radiation doses affect the mechanical properties and morphological characteristics of a manufactured one-mix geopolymer made from significant quantities of basalt waste as a distinctive and environmentally friendly cementitious material. One-mix geopolymer is more likely to be utilized as a cement substitute with the suggested method. In order to improve its performance and durability against high temperatures, gamma radiation, and sulfate attack, manufactured GP was reinforced with 0.5 and 1.0 wt.% nano-TiO$_2$.

Experimental

Materials characterization

The following materials were adopted in this study:

- Ground granulated blast-furnace slag (GGBFS), a precursor for aluminum-silicates that is rich in calcium, was used. It was originated from an iron and steel factory in Helwan, Egypt. It has a 2883 cm^2/g Blaine-specific surface area.
- The crushed basalt came from the Shuq El-Thouban, Egypt. It was ground and sieved to particles with a Blaine surface area of 2643 cm^2/g and particle size of $\leq$ 45-mm basalt waste (BW).
- Figure 1 shows XRD patterns of BW and GGBFS and BW as determined by XRD instrument (model Xpert-2000, Philips), whereas Table 1 presents the mineralogical oxide compositions of BW and GGBFS as determined by X-ray fluorescence spectrometer (XRF, model PW-1400, Xios).
- A significant hump can be observed in the X-ray diffractograms of GGBFS between $2\theta = 23-36°$, which is connected to material's amorphous nature, whereas XRD patterns for BW reveal distinct peaks for quartz (SiO$_2$) at $2\theta = 22.8, 26.3, 29.0, 37.0, 39.9$, and $41.0°$ (*PDF*: 00–005-0490); illite at $2\theta = 28.6, 31.1, 33.2, 35.6, 41.0$, and $42.8°$ (*PDF*: 00–001-0614); and calcite at $2\theta = 30.1, 43.0$, and $48.1°$ (*PDF*: 01–088-1808) [33]. The TS25 standard, which designates the pozzolanic material, is applicable to BW based on the chemical oxide percent data presented in Table 1. The TS25 standard assumes that the summation of SiO$_2$ + Al$_2$O$_3$ + Fe$_2$O$_3$ wt.% should be $\geq$ 70%, Cl$^-$ content $\leq$ 1%, SO$_3$ content $\leq$ 3%, and the reactive silica content not less than 25% [42].
- Alkaline activators which include sodium hydroxide (NaOH) and sodium silicate (Na$_2$Si$_2$O$_3$) were purchased commercially from Al-Salam Association, 6 October District, Egypt. The dry mix of GP was supplemented with 5 and 10 wt.% of NaOH and Na$_2$Si$_2$O$_3$, respectively, from the weight of the mix and one-part mix [9, 10].
- Nano-TiO$_2$ (NT) with a purity of 99% and density of 0.04–0.06 g/ml was delivered from Al-Salam Association, 6 October District, Egypt. Surface characteristics of NT were examined via interpreting N$_2$-adsorption/desorption isotherm 77 °K (Fig. 2a, b).
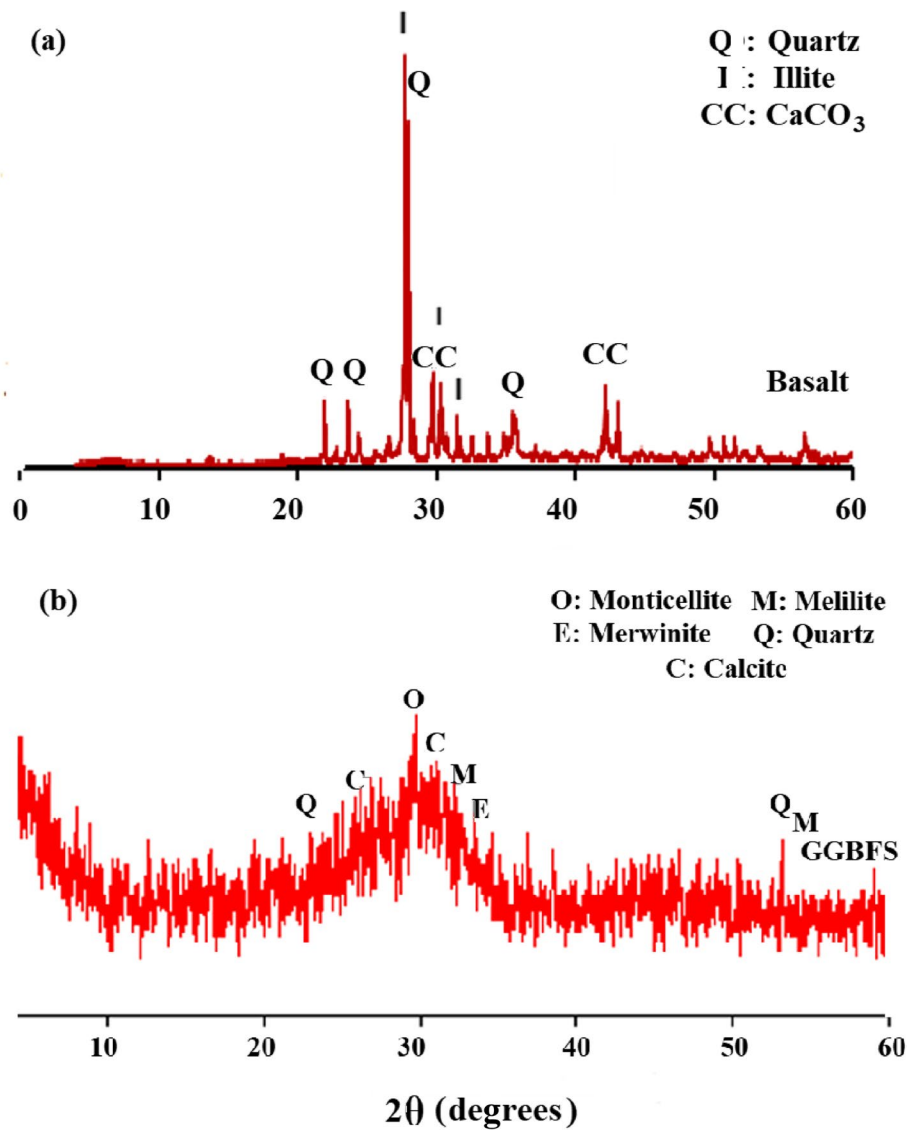
Fig. 1 XRD patterns of **a** basalt and **b** GGBFS

Table 1 Chemical oxide composition of the raw materials

Oxide (%)	BFS	WB
Al_2O_3	7.11	14.18
CaO	35.38	8.35
SiO_2	38.33	60.10
Fe_2O_3	2.96	7.11
MgO	5.40	4.62
K_2O	0.76	0.97
Na_2O	0.28	2.49
SO_3	1.29	0.00
Cl^-	0.01	0.00
LOI	9.49	1.90
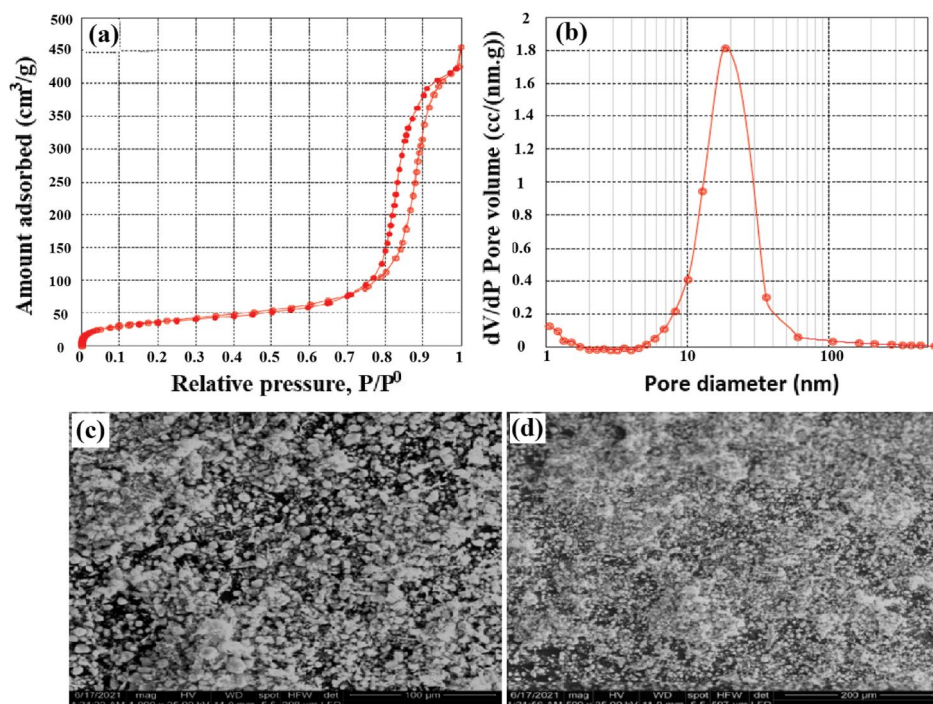
Fig. 2 **a** Adsorption–desorption isotherm, **b** BJH curve, and **c** & **d** SEM images of NT

The adsorption/desorption isotherm of nano-TiO_2 (NT) is identified as a type 2 with a small H1 hysteresis loop according to IUPAC classifications. As shown by the monolayer capacity (V_m) of 2.0 cm^3/g and the average pore diameter of 28.29 nm, the pores in NT are in the meso/micro range. Additionally, the total pore volume (Vp) was determined to be 0.0616 cm^3/g, and the BET surface area (S_{BET}) for nano-TiO_2 was estimated to be 87.15 m^2/g. On the other hand, Fig. 2b shows Barrett-Joyner-Halenda (BJH) curve of pore size distribution by volume for NT. The majority of the NT pores are evidenced to be mesopores according to the data of Fig. 2b, where $dp_{max} = 40$ nm. SEM micrographs of nano-TiO_2 illustrated in Fig. 2c reveal that the NT particles are extremely tiny and spherical, with a consistent size distribution and a diameter that varied from 20 to 80 nm.

GP mix design

Along with the TiO_2 nanoparticles, two precursors were used in the current investigation. Various dry blends were developed by substituting GGBFS by 0, 20, 40, and 60 wt.% BW. The solid alkaline activators were added to the dry blend at a rate of 15 wt.% (5% NaOH, 10% $Na_2Si_2O_3$) of the total mass. To guarantee the homogeneity of the mix, each dry mix (containing the dry raw precursors and the solid activators) was stirred for 6 h in a porcelain ball mill. Designation and composition of the examined dry mixes are disclosed in Table 2.

Each dry mix was mixed with water to create geopolymer pastes. All of the created pastes had the same consistency, suggesting that substituting BW for GGBFS did not affect the workability of GP paste as well as the water/solid (W/S) ratio necessary for standard consistency. To assure the uniform distribution of the nanoparticles in the

Mashout *et al. Journal of Engineering and Applied Science*   (2023) 70:106

Page 6 of 24

Table 2 Mixes notation and their composition

Mix	Composition (wt,%)	Si/Al	Ca/Si
M	100% BFS	5.45	0.92
M20	80%BFS + 20% WB	5.31	0.83
M40	60%BFS + 40% WB	4.91	0.711
M60	40%BFS + 60% WB	4.17	.0.69
M20-T1	80%BFS + 20% WB + 0.5% NT	5.31	0.83
M20-T2	80%BFS + 20% WB + 1% NT	5.31	0.83

mixing water within the pastes containing nano-TiO_2, they were initially suspended in a mixture of water along with 3 wt.% superplasticizer, and the suspension was sonicated by ultrasonic homogenizer (LUHS0A12, 650W, 220 V/50HZ) for 1 h [43]. To begin the geopolymerization processes, the dry mixes were combined with water, and the resulting pastes were molded into cubic specimens utilizing one-inch cubic molds and kept overnight at $RH \approx 98 \pm 2\%$.

The hardened cubic specimens were taken out of the molds after 24 h and were cured under humid conditions ($\geq 99\%$) to retain the geopolymerization processes [44].

Testing routine

According to ASTM C191, the Vicat apparatus was used to measure the initial and final setting times for all the freshly developed geopolymer pastes [41]. This apparatus comprises a frame that contains a mobile rod, equipped with a disc at one side and a needle that can be affixed at the opposite end.

Compressive strength tests were done using a Ton Industrial Machine (West Germany) for maximum load of 60 tons. The test was performed on three cubic specimens, for each geopolymer mix, after 3, 14, 28, and 90 days to monitor the strength that had evolved, according to ASTM C109 M16-a [13, 45].

After 3 and 28 days of curing, total porosity (P, %) and bulk density (BD, g/cm^3) were performed by measuring the following weights of the hardened cube that represent each GP mix: the weight of the cube suspended in air (saturated surface dry) (W1), its weight immersed in water (W2), and then the weight of the cube after drying at 100 °C for about 24 h (W3). Bulk density and total porosity were calculated using formulae 1 and 2:

$$\text{Bulk density (B.D)} = \frac{W1}{W1 - W2} \tag{1}$$

$$\text{Porosity (P\%)} = \frac{W1 - W3}{W1 - W2} \tag{2}$$

Durability tests

Fire resistance

The thermal resistance test was performed on the 28-day cured samples. Three cubes which represent each GP mix were dried in an oven at 90 °C overnight. They were then fired for 3 h at temperatures of 250, 500, and 750 °C in a muffle furnace at a heating rate

of 10 °C per minute. The burned specimens were tested for compressive strength after being cooled progressively to room temperature in desiccators. Applying Eq. 3, residual strength $(RS)_t$ was evaluated.

$$(RS)_t = \frac{(C.S)t}{(C.S.)0} \times 100 \tag{3}$$

$(C.S)_t$: Compressive strength after firing.
$(C.S)_0$: Compressive strength after 28-day hydration.

Sulfate attack test

Three cubes for each GP mix, after hydration for 28 days, were submerging in $MgSO_4$ solution (7%) for up to 4 months, to evaluate the detrimental effects of sulfate ions penetration. Samples were removed after 1, 2, and 4 months of curing in sulfate solution, and their compressive strength was evaluated, and the average value was adopted.

Irradiation by γ-rays

Resistance of GP mixes to irradiation of *γ*-rays was tested by exposing the dried 28-day samples to a gamma-ray source (Co^{60}, dose rate 985 kGy/*h*) applying 500, 1000, and 1500 kGy with a dosing rate 1.4 kGy/*h*. After irradiating the samples, the compressive strength test was assigned after the sample had been exposed to radiation, and the residual strengths (RS %)$_{rad}$ were determined using Eq. 4:

$$(RS\%)_{rad} = \frac{(CS)rad}{(CS)0} \times 100 \tag{4}$$

Where CS_{rad} is the compressive strength after radiation given dosage of *γ*-ray, CS_0 is the compressive strength prior to radiation (28-day value).

Phase composition and microstructure

GP phases that developed during the hydration of the various geopolymer specimens were identified using XRD and thermogravimetric techniques. XRD was performed using cobalt target ($\lambda = 0.17889$ nm) and filter made of nickel under 40 kV and 40 mA. The scanning range spanned from 5 to 60 (2θ°), with a scanning speed of 1 s/step and a resolution of 0.02/step. TGA test was done using TGA:TA instrument, model SDT Q600. A nitrogen environment was maintained while heating 15 mg of powdered sample (≤ 25 μm) in the temperature range of 50 to 1000 °C, with a heating rate of 10 °C/min. The microstructure of various GP samples was explored using SEM-Quanta 250 FEG equipment.

Results and discussion

Setting times

Setting times are thought to be crucial factors that can impact how the tested materials are handled and what applications they can be used for [9]. The initial and final setting times of geopolymer mixes without and with basalt are shown in Fig. 3. Initial and final setting times are found to be 25 and 44 min, respectively, for the geopolymer mixture consisting entirely of GGBFS (mix M). One-part geopolymer sets up more quickly than
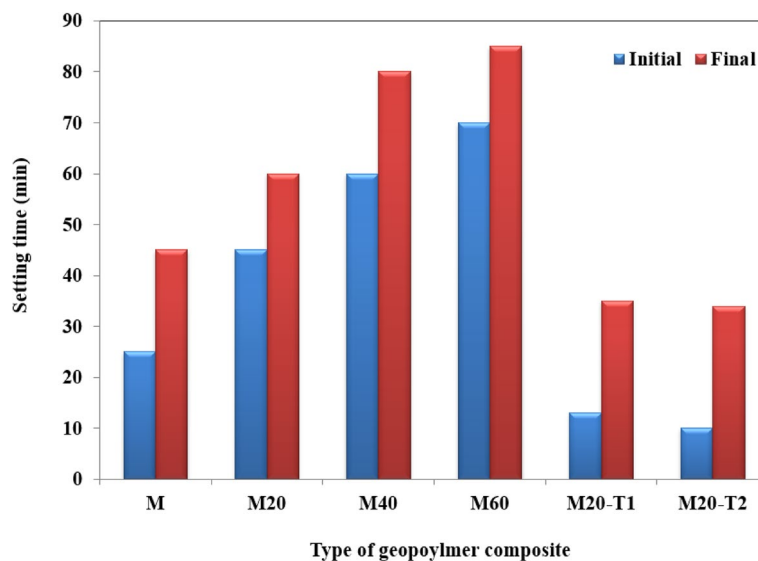
Fig. 3 Setting times of the various GP composites

OPC owing to the heat released during the solid NaOH activator's dissolution [46]. Furthermore, the interaction between GGBFS and alkaline activators is an exothermic reaction in which the produced heat promotes the geopolymerization process [47].

Replacement of GGBFS by BW causes an enlargement in the setting time. Additionally, the enlargement of setting times becomes greater as replacement percentage of BW increases, reaching about 280% for the initial and 190% for the final setting times for mix M60 (40% GGBFS + 60% BW compared to control mix (M, 100% GGBFS). This discovery is consistent with earlier research and may be explained by the fact that the geopolymer mixture's Si/Al ratio decreased as the basalt percentage increased which is a crucial factor in governing both setting times and compressive strength measurements [48]. Table 2 shows that the Si/Al ratios for M, M20, M40, and M60 are 5.45, 5.31, 4.91, and 4.17, respectively. The quantity of soluble Si that stimulates the geopolymer reaction is decreased by lowering the Si/Al ratio [34]. However, these blended mixes exhibit setting times that are satisfactory for the ASTM-C150M standards, demonstrating the proper application of these geopolymer blends as an alternative to conventional OPC [49].

Furthermore, setting times significantly decrease by adding 0.5 or 1% of nano-titanium oxide (NT) to mix M20 (80% GGBFS + 20% BW). Evidently, seeded nucleation occurs due to NT particles' dispersion in the one-part geopolymer matrix [50]. According to Hajimohammadi et al. [51], this nucleation inhibits Al from adhering to silica particles, which regulates silica release and speeds up the development of products with high silica phase content in the early geopolymerization processes.

Compressive strength

The strength of any cementitious component determines its appropriateness as a construction material. Figure 4a shows the compressive strength variation for mixes M, M20, M40, and M60 with geopolymerization time. As the curing period increases, the compressive strength of the control mix (100% GGBFS, mix M) increases continuously,
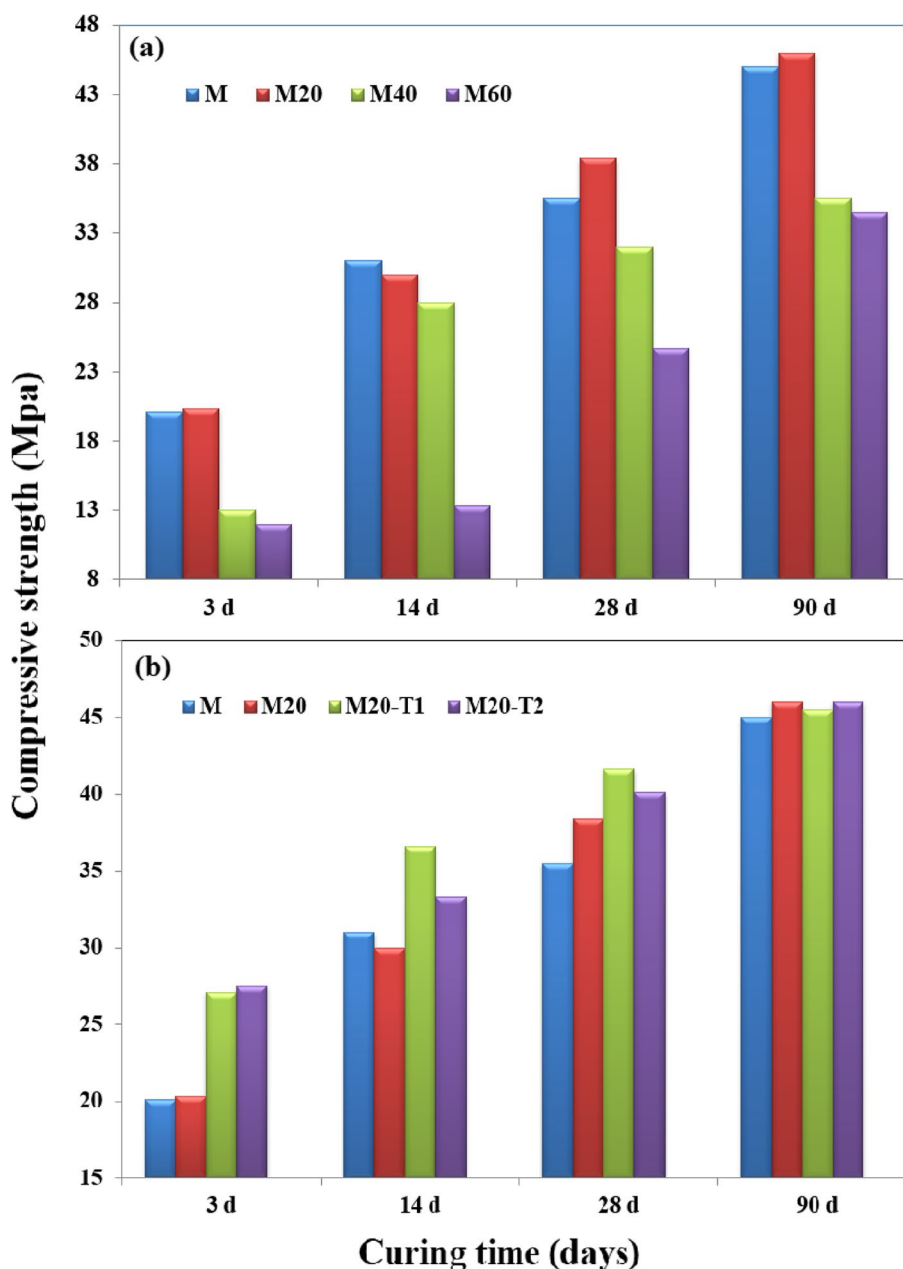
Fig. 4 Compressive strength (MPa) of the various GP composites. **a** Without and **b** admixed with NT

and around 66% of the strength is gained in the first 14 days. This is derived from the partial disintegrating of GGBFS particles caused by the action of the alkaline activator. This disintegration encourages the release of active species like Ca^{2+}; $[H_2SiO_4]_2^-$, $[H_3SiO_4]^-$, and $[Al(OH)_4]^-$. These species operate as monomers, initiating geopolymerization reactions that result in strength-giving phases like CSH and CASH gels [13, 52]. The gained strength often diminishes when GGBFS is replaced by BW. As the BW percentage is increased from 20 to 60% in the mix, the strength decreases. This occurs because of the replacement of slag (a material with a high calcium content) with BW (a substance with a high silica content), which results in the creation of hydration products

like sodium aluminosilicate hydrate (NASH) gel [53]. NASH has weaker binding characteristics than calcium silicate hydrate (CSH) gel [54]. Nevertheless, mix M20 exhibits higher strength at 28 and 90 days than the control mix, whereas mix M40 and M60 provide CS at 28 and 90 days that are around 70% of control values. This demonstrates that the M20 mix represents the optimal ratio of soluble Ca^{+2} ions provided by GGBFS which interacts with silicate ions from BW leading to the formation of an extra gel that provides strength [55].

Figure 4b shows the compressive strength of geopolymer blends comprised of 80% GGBFS + 20% BW and admixed with 0.5 or 1% nano-TiO_2 (M20-T1 and M20-T2, respectively). Evidently, the strength of M20-T1 and M20-T2 composites is improved when compared to M and M20, especially at early curing ages. Such finding is consistent with the outcomes of setting times and may be relevant to the following: (i) the effective dispersion of NT in the matrix of geopolymer and (ii) the substantial surface area (87.15 m^2/g) and superior fineness ($\sim$20–80 nm) for NT. The combination of the above factors causes the geopolymerization of the precursor materials to start rapidly. Additionally, due to their filling activity, NT tiny particles reduce porosities and serve as catalysts for geopolymerization reactions. Combining these traits causes the hydration products with strong binding characteristics to accumulate, increasing the strength [42, 45, 56].

Bulk density and porosity (%)

The variation of the geopolymer system's bulk density (BD, g/cm^3) and porosity (P, %) with curing time is an indication of the progress of the polymeric reactions and hence the strength development. Figure 5a and b shows the BD and P% of M, M20, and M20-T2 mixes with compressive strength after 3 and 28 days of curing. Deposition of the various geopolymerization products leads to a subsequent clogging of the accessible pores (reduction in P%) and an increase in the bulk density from 3 to 28 days in all investigated mixes. After 3 days, the blended mix (M20) possessed higher porosity and lower BD than the control mix (M), and after 28 days, the behavior changed, showing that the geopolymer system's produced hydrates have changed in both quantity and type as a result of the partial replacement of GGBFS by BW [57]. Such behavior is in line with the obtained compressive strength of these two combinations. Among the examined mixes, M20-T2 composites had the lowest P% and the greatest BD and CS after 3 and 28 days, indicating that this composite has the best-consolidated structure. This demonstrates how the nanoparticles serve to speed up the geopolymerization process, especially in the early stages [58].

Durability tests

Fire test

Figure 6 shows the residual strength (RS)$_t$ for specimens M, M20, M40, and M20-T2 upon fire at 250, 500, and 750 °C for 3 h and progressive cooling to ambient temperature in desiccators, and Fig. 7b shows the visual appearance of GP samples after firing at 500 °C. Evidently, firing at 250 °C boosts compressive strength for M, M20, M40, and M20-T2 by 10, 12, 5, and 22%, respectively, compared to their strengths at 28 days. The unreacted GGBFS grains and the alkaline hydroxyl anions are activated by heating the hardened geopolymer mix at 250 °C, which increases the steam
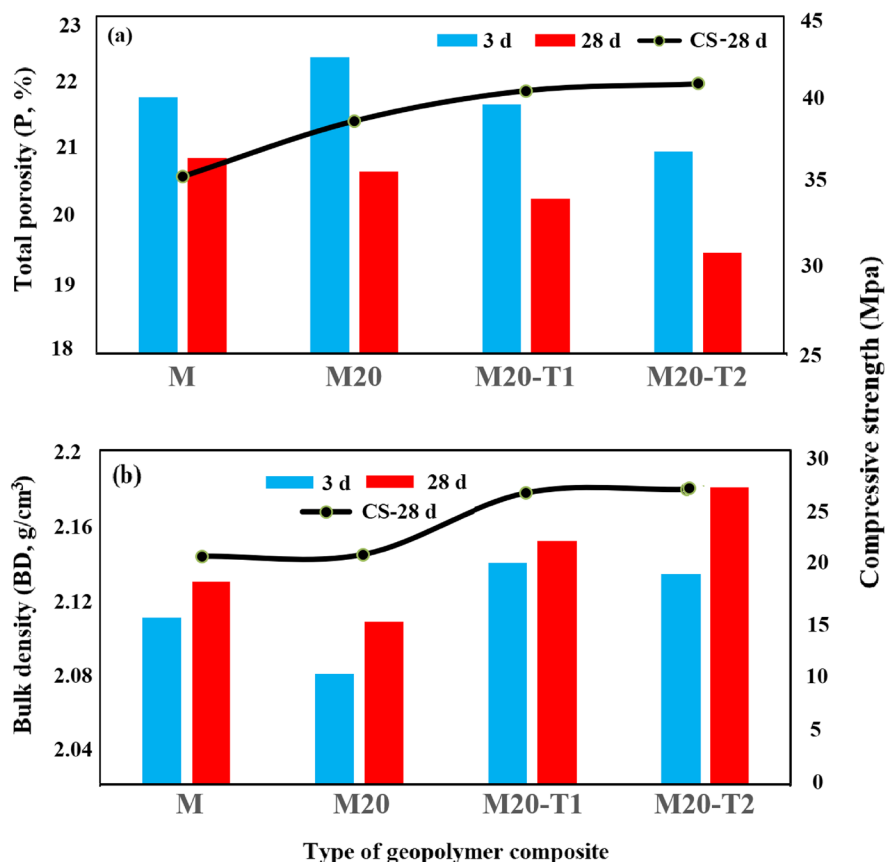
Fig. 5 Correlation between **a** total porosity (P, %) and **b** bulk density (BD, g/cm³) with compressive strength of GP composites after 3 and 28 days of curing

pressure inside the geopolymer matrix and continues the hydration and geopolymerization processes [30, 43, 58]. As a result, additional binding products such as CSH gel, CASH, NSAH, and NCASH will be generated. The aggregation of these compounds improves the geopolymer mix's mechanical characteristics. These outcomes agree with earlier publications [59, 60]. Compressive strength for the M, M20, and M40 mixes decreased slightly after firing at 500 °C by 8.3, 4.2, and 14.8%, respectively, yet the composite M20-T2 still gained strength by around 5% exceeding its 28-day value. When GP is heated to 500 °C, the geopolymer matrix suffers thermal degradation, and the unstable phases dissolve, resulting in low $(RS)_t$%. This decrease in $(RS)_t$ is mostly dependent on the type and/or quantity of geopolymer hydrates, which is connected to the constitution of the starting precursors. This explains the variations in $(RS)_t$ across the studied mixes. However, the M20-T2 composite's RS_t at 500 °C is still greater than its original value after 28 days of hydration, indicating the presence of additional quantities of hydrates with reduced porosities and the contribution of NT particles to the improvement of this composite's thermal stability [61, 62]. Upon firing at 750 °C, all GP mixes show a significantly decrease in compressive strength. RS_t for M, M20, M40, and M20-T2 mixes were 46.2, 41, 53.2, and 22%, respectively. Evidently, at 750 °C, dehydration/dehydroxylation of all the produced hydrates took
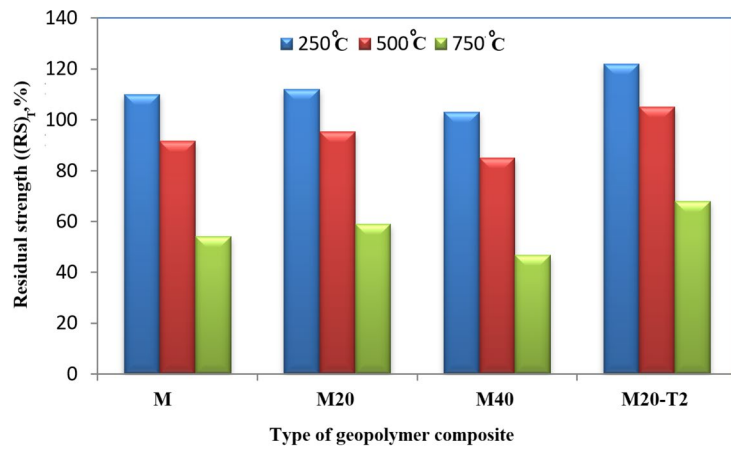
a: Residual strength (RS)$_T$ of GP composites after firing at 250, 500 and 750 °C.
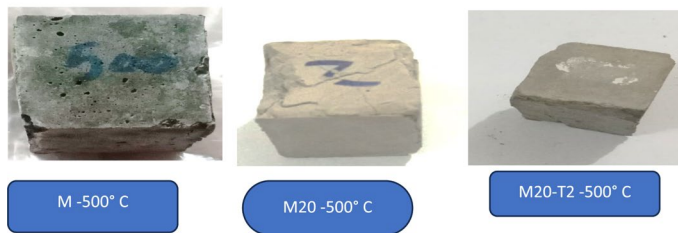
b: visual appearance of GP mixes after firing at 500° C

Fig. 6 **a** Residual strength (RS)$_T$ of GP composites after firing at 250, 500, and 750 °C. **b** Visual appearance of GP mixes after firing at 500 °C

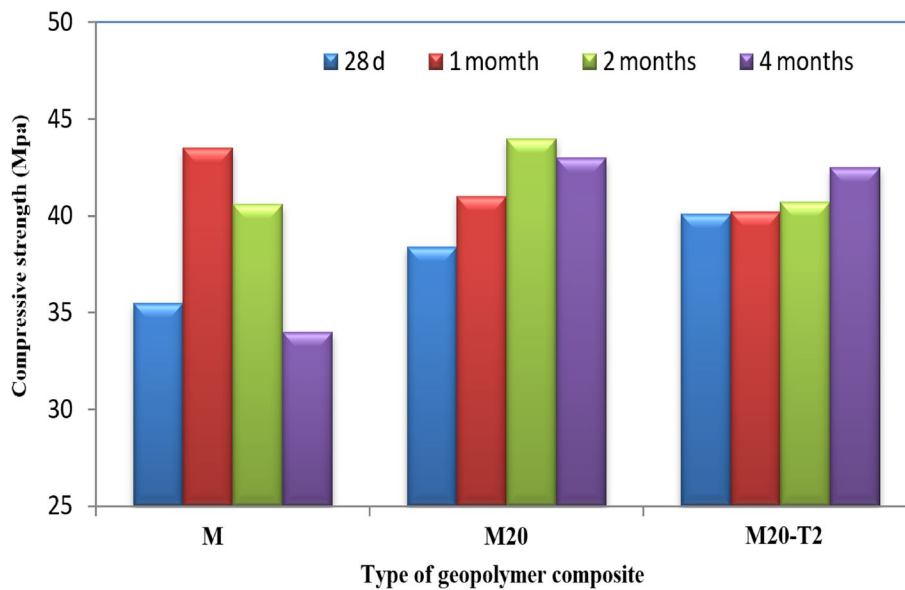**Fig. 7** Compressive strength of GP composites after various periods of curing in MgSO$_4$ solution

Mashout *et al. Journal of Engineering and Applied Science* (2023) 70:106

Page 13 of 24

place, causing the pore matrix's high pressure to create microcracks, which greatly diminished the mixes' mechanical characteristics as well as their residual strengths $(RS)_t$. Again, at this high temperature, mix M20-T2 experiences the least strength loss. Such findings will be validated by XRD and SEM analyses, which will be presented in the next sections.

SO_4^{-2} ions penetration

M, M20, and M20-T2 mixtures were subjected to the attack by SO_4^{2-} ions test by submerging the samples in $MgSO_4$ solution (7%) for up to 4 months. Figure 7 illustrates the results of the compressive strength measurements at 1, 2, and 4 months of immersing in $MgSO_4$ solution. For the three examined mixes, the behavior of GP mixes in $MgSO_4$ solution exhibits different tendencies. In the first month of curing, mix M showed an increase in CS, followed by a progressive failure in strength. M20 mix showed a similar trend, but the boosting in CS extended to 2 months of immersion. However, the CS of M20-T2 remained almost unaltered for the first 2 months before increasing after 4 months of curing. Attack of any hardened cementitious material (CSH or CASH) by SO_4^{-2} ions is resulting in the development of expansive hydration products like Ettringite [63, 64]. The accumulation and precipitation of these hydrates inside the pores can improve the strength after short time of attack by sulfate ions. Meanwhile, as we observe in mix M, the accumulation of these hydrates causes internal stress and the creation of fractures owing to continual immersion in sulfate ions [65]. The nature of hydration products produced in the hardened mix and its pore system primarily determine the degree to which CS is deteriorated by SO_4^{-2} attack. The resistance of this mixture to strength depletion driven on by attack by SO_4^{-2} ions is explained by the improved pore system in M20-T2. Similar observations were made with fly ash-based geopolymer concrete, which indicated that there was less of a loss in CS following immersion in solutions of sulfate and chloride [47, 66].

Shielding test

The shielding characteristics of any construction material are critical in determining its potential use in a wide range of applications. Figure 8a shows the residual strength $(RS)_{rad}$ % of mixes M, M20, and M20-T2 after exposure to a γ-ray source (^{60}Co-γ-cell-220, Atomic Energy Commission, Canada) with varying intensities (500, 1000, and 1500 kGy), while Fig. 8b depicts the visual appearance of GP samples after 1500-kGy irradiation. Obviously, increasing the power of an irradiated gamma ray reduces $(RS)_{rad}$, for all the studied GP mixes, suggesting the destructive characteristics of irradiated rays to target hydration products and a subsequent negative influence on compressive strength [67, 68]. When compared to the control (mix M), mix M20 exhibits a resistant behavior, particularly at high irradiating doses of 1000 and 1500 kGy. This finding can be related to the hydration/geopolymerization products created in mix M20 (low Ca ion and high Si/Al ratio) as opposed to those formed in mix M (control). According to Al-Hamarneh [69] and Lambertin et al. [70], irradiation can readily create additional binding phases by cross-linking the aluminosilicate's linear chains. Incorporating 1% nano-TiO_2 into M20-T2 composite had a beneficial effect on the mix's shielding characteristics at all the measured γ-ray dosages, as evidenced by the high residual strength
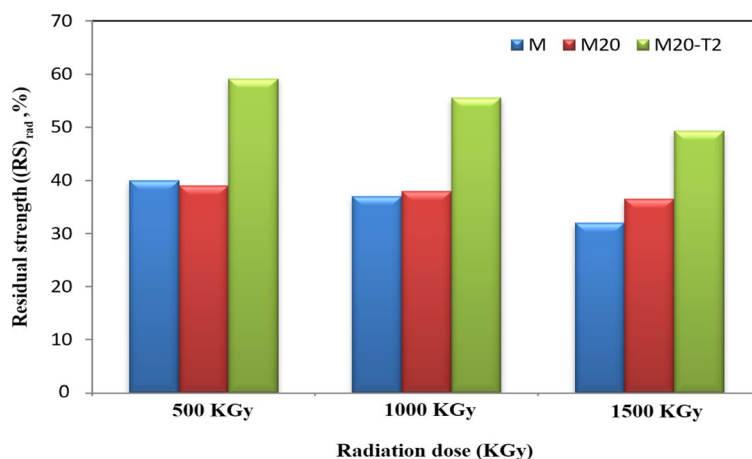
a: Residual strength (RS)$_{rad}$ of the various GP composites after
irradiating by various doses of gamma-rays

b: visual appearance of various samples after irradiating by 1500KGy

Fig. 8 **a** Residual strength (RS)$_{rad}$ of the various GP composites after irradiating by various doses of gamma rays. **b** Visual appearance of various samples after irradiating by 1500 KGy

(RS)$_{rad}$. The shielding resistance in this case is due to the greater hydration gel generated in this composite compared to M or M20. Actually, NT particles operate as an activator, promoting geopolymerization and generating more gel-binding products.

Phase composition

XRD

XRD patterns for mixes M and M20 after 3 and 28 days of geopolymerization processes are shown in Fig. 9. XRD diffractograms of mix M after 3 days of geopolymerization displayed peaks at $2\theta = 29.54°$ (PDF nos. 00–033-0306, 00–034-0002) and 32.21° (PDF no. 00–020-0452), which could be attributed to CSH gel and hydrogarnet (CASH), respectively, as the principal hydration products [13, 68]. The occurrence of such phases in the geopolymer network of M mix can be attributed to an excessive amount of Ca^{+2} ions derived from GGBFS. It has been terminated that the presence of calcium ions induces the precipitation of CASH, which serves as nucleation sites for geopolymerization process [71]. Additionally, CSHs and CASH established an essential framework of percolating solids that triggered the hardening process [72]. Furthermore, peaks of the illite phase and unreacted quartz ($2\theta = 29.64°$) appeared.

Nevertheless, the XRD pattern of mix M20 (80% GGBFS + 20% BW) after 3 days of geopolymerization shows peaks for new hydration products, specifically garronite (NCASH) at $2\theta = 32.2°$ (PDF no. 01079–2424) and tetragonal Na-alumino-silicate hydrates (NASH) at $2\theta = 27.8°$ and 32.1° (NASHs, PDF nos. 00–039-0217 and

Mashout *et al. Journal of Engineering and Applied Science*   (2023) 70:106
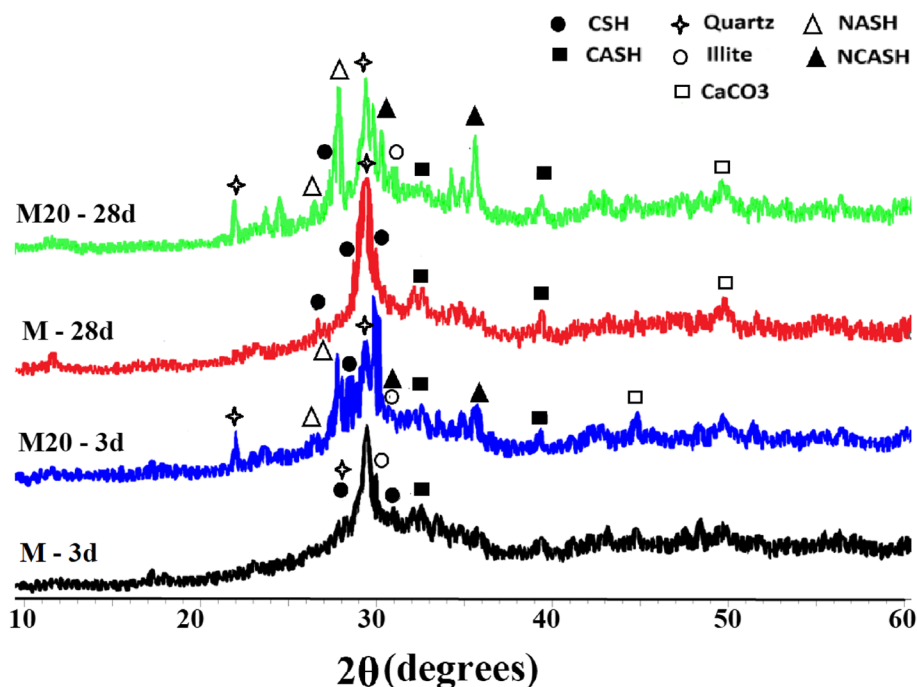
Page 15 of 24

Fig. 9 XRD patterns of mixes M and M20 after 3 and 28 days of curing

00–026-1382) [73]. The production of these phases is influenced by the Si/Al ratio in the polymeric system as well as the cations obtained from the alkaline activator. As previously mentioned, NCASH may arise in a polymeric system as a result of the transition of gismondine, a highly calcium-rich phase, into NCASH via the exchange of Ca^{2+} ions for Na^{+} ions in a highly concentrated alkaline medium [59]. After 28 days, the peak intensities of the hydrated phases for mixes M and M20 grew, while those of the unreacted phases dropped indicating the continuity of polymerization processes.

XRD patterns of mixes M and M20 upon firing at 250 °C and 750 °C, are shown in Figs. 10 and 11, respectively. The sharpness of the peaks associated with CSH gel and (CASH) increases in the XRD pattern of mix M at 250 °C, demonstrating the rise in quantities of these products during the self-autoclaving process [66]. However, burning at 750 °C causes nearly disappearance of hydrated phases, as evidenced from the XRD pattern, and dehydrated phases like gehlenite ($Ca_2Al_2SiO_7$, PDF no. 01–079-2423) appeared, which have poor mechanical characteristics (Fig. 11). Similar findings to those of mix M can be seen in the XRD patterns of M20 at 250 °C, where there is a reduction in the intensities of NASH-related peaks. At 750 °C, however, additional peaks in the XRD pattern can be observed that may be connected to sodium-rich phases which are thermally stable, such as nepheline ($NaAlSiO_4$, PDF no. 01–070-1582) [74].

Figure 12 shows XRD diffractograms of composite M20-T2 after 3 and 28 days of geopolymerization as well as after firing at 250 °C and 750 °C. Evidently, mix M20-T2 showed the identical peaks of mix M20 with relatively high intensities and almost no unhydrated phases, demonstrating that the NT dispersion in the geopolymer matrix enhances and speeds up the hydration/geopolymerization processes [75, 76]. This also implies that several hydrated products, such as CSH, CASH, and NASH, continued to
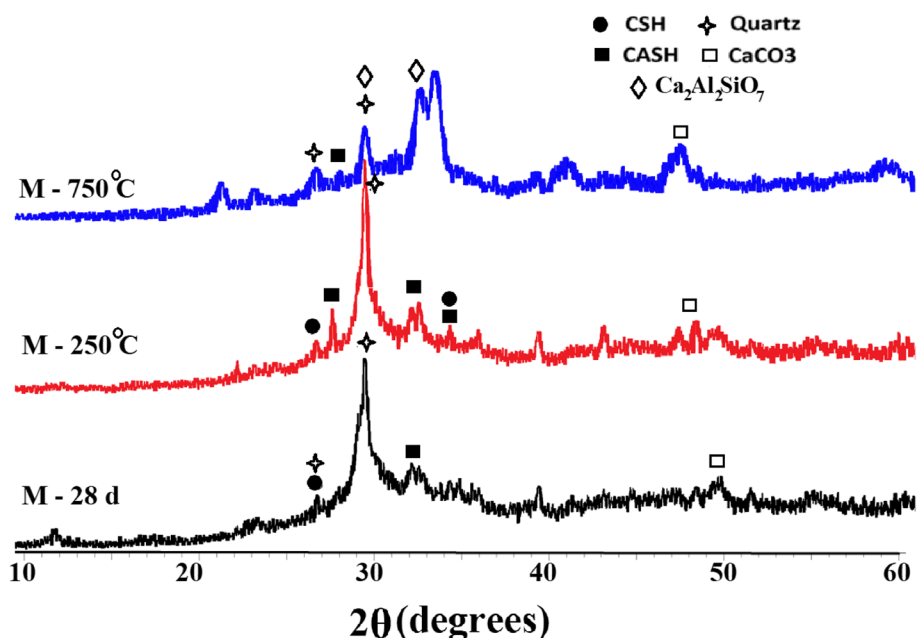
Mashout *et al. Journal of Engineering and Applied Science*　(2023) 70:106

Page 16 of 24

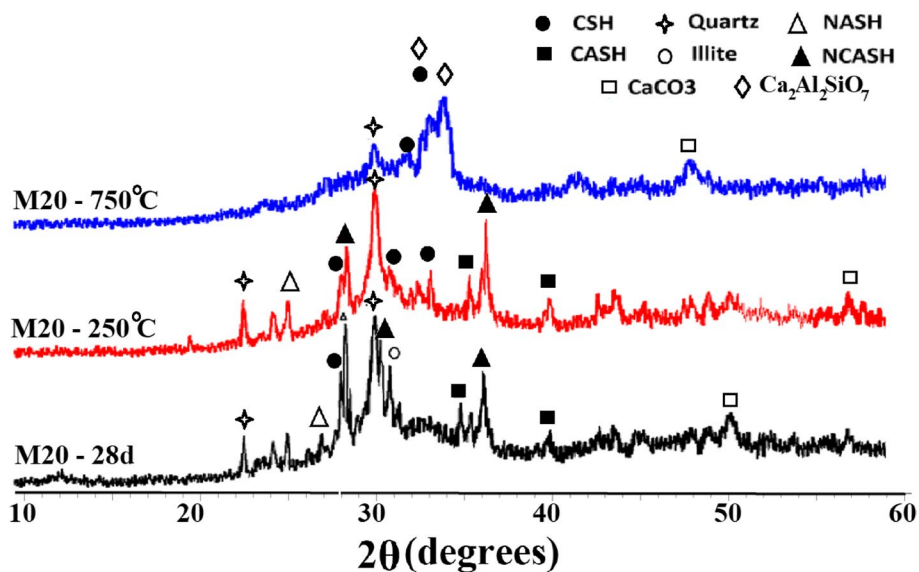**Fig. 10** XRD patterns of mix M after firing at 250 and 750 °C

Fig. 11 XRD patterns of mix M20 after firing at 250 and 750 °C

exist at firing temperatures of 250 and 750 °C, indicating the thermal stability of M20-T2 composite at these two temperatures.

TGA

TGA diagrams for mixes M, M20, and M20-T2 after 3 and 28 days of geopolymerization are shown in Fig. 13a and b, respectively. A progressive mass loss by heating to 1000 °C is observed for the three mixes after 3 days. The mass loss percentages (%) for M, M20, and M20-T2 were 6.19, 7.73, and 8.53%, respectively, reflecting the quantities of
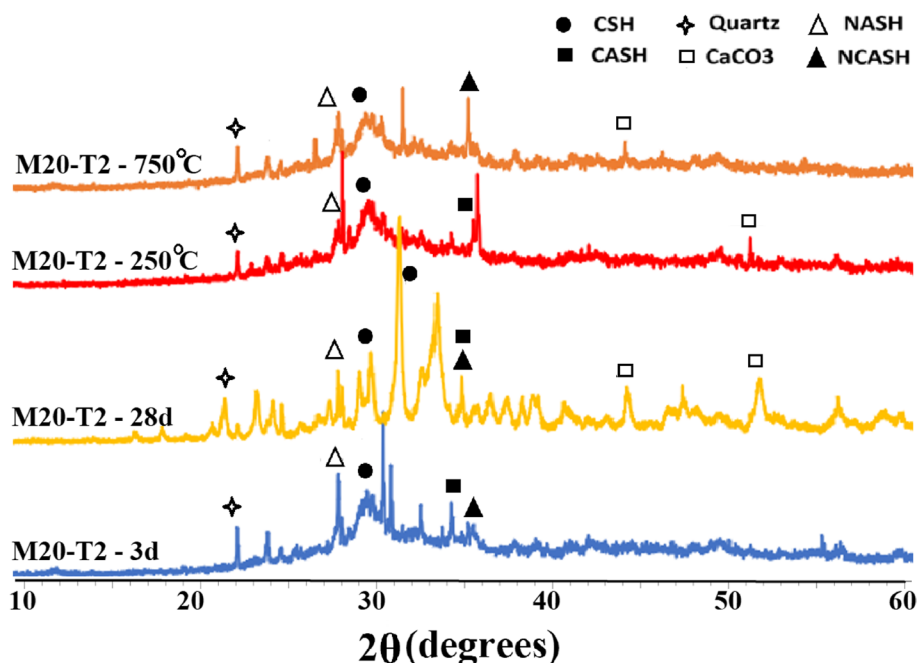
Fig. 12 XRD patterns of mix M20-T2 after 3 and 28 days of curing and after firing at 250 and 750 °C

hydration/geopolymerization products produced in these mixtures. M20-T2 offers the highest amounts of hydrates among all mixes which confirm the catalytic role of NT to promote the geopolymerization reactions. The mass loss in the three samples is detected at three temperature stages: 50–300°, 300–600°, and 600–950 °C. Table 3 shows the mass loss % for all mixes at various stages. The first stage of mass loss occurs between 50 and 300 °C and is due to the release of unbinding water as well as the partial disintegration of CSH and CASH gels. The second stage, which accounts for the main of mass loss, occurs between 300 and 600 °C and is triggered by the dehydroxation of hydrogrant (C_3ASH_4) and hydrotalcite ($Mg_6Al_2(CO_3)(OH)_{16} \cdot 4H_2O$) [73]. Nevertheless, the third stage, which experiences the least mass loss %, is associated with decarbonation of $CaCO_3$, which occurs as a consequence of carbonation of the samples during handling [77]. All samples possessed an increase in mass loss % after 28 days of curing, suggesting that the geopolymerization processes were progressing. For mixes M, M20, and M20-T2, the respective mass loss percentages were 8.31, 10.27, and 10.0%.

Microstructure

SEM micrographs of mixes M, M20, and M20-T2 after 3 and 28 days of curing are shown in Fig. 14((a1, a2), (b1, b2), and (c1, c2)), respectively. After 3 days, the SEM picture of the mix M shows a semi-compact structure with unreacted spherical slag particles and solid alkaline activator (as hexagon plates) as well as newly developed phases such as short CSH gel and cubic plates of CASH (Fig. 15a1) [78]. The mixture got more solidified after 28 days due to the deposition of hydrates, which formed a cylinder of geopolymer chains that joined the unreacted slag particles (Fig. 15a2). Such photos demonstrate the geopolymerization process's development and explain
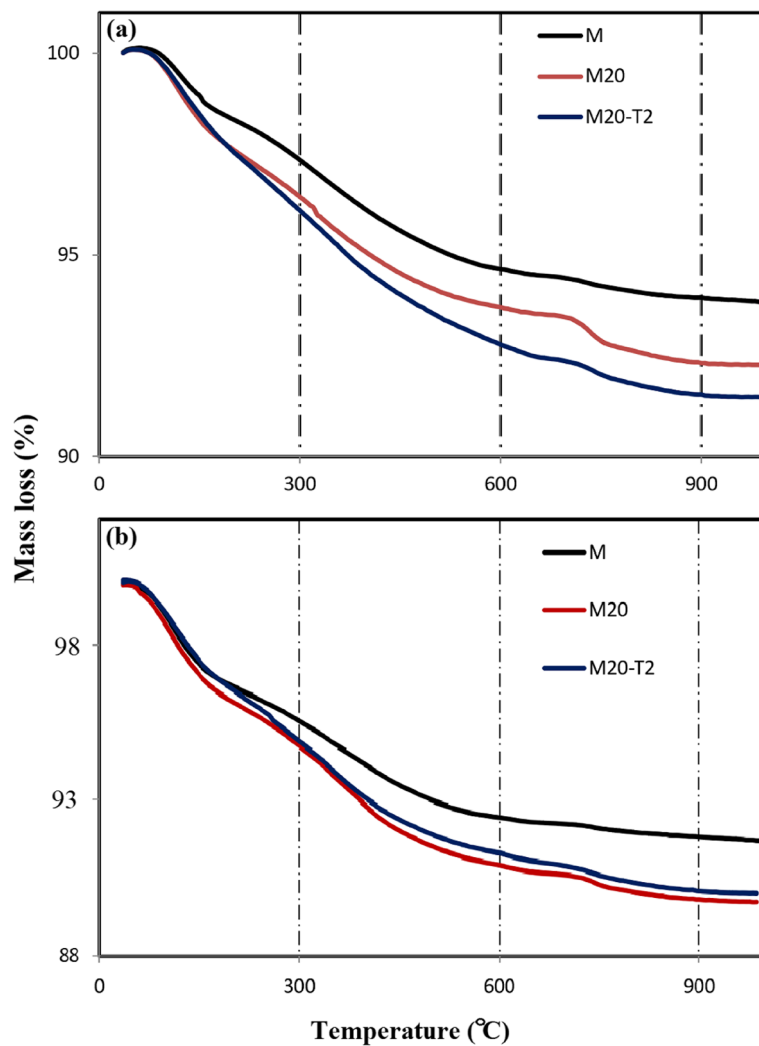
Fig. 13 TGA curves for the various mixes after **a** 3 and **b** 28 days of curing

Table 3 Mass loss % of various GP mixes

Mix	Mass loss %			Total mass loss %
	Temperature range			
	50–300 °C	**300–600 °C**	**600–950 °C**	
M, 3 days	1.5	4.5	0.35	6.19
M, 28 days	3.6	4.13	0.57	8.3
M20, 3 days	2.99	4.3	0.37	7.73
M20, 28 days	3.99	5.26	0.78	10.27
M20-T2, 3 days	3.83	4.54	0.16	8.53
M20-T2, 28 days	3.77	5.25	0.10	10.0

the improvement in mechanical characteristics. For mix M2, analogous observations are seen after 3 and 28 days (Fig. 14b1, b2, respectively). When comparing the geopolymer matrix for mix M20-T2 composite to those of mixes M and M20, SEM
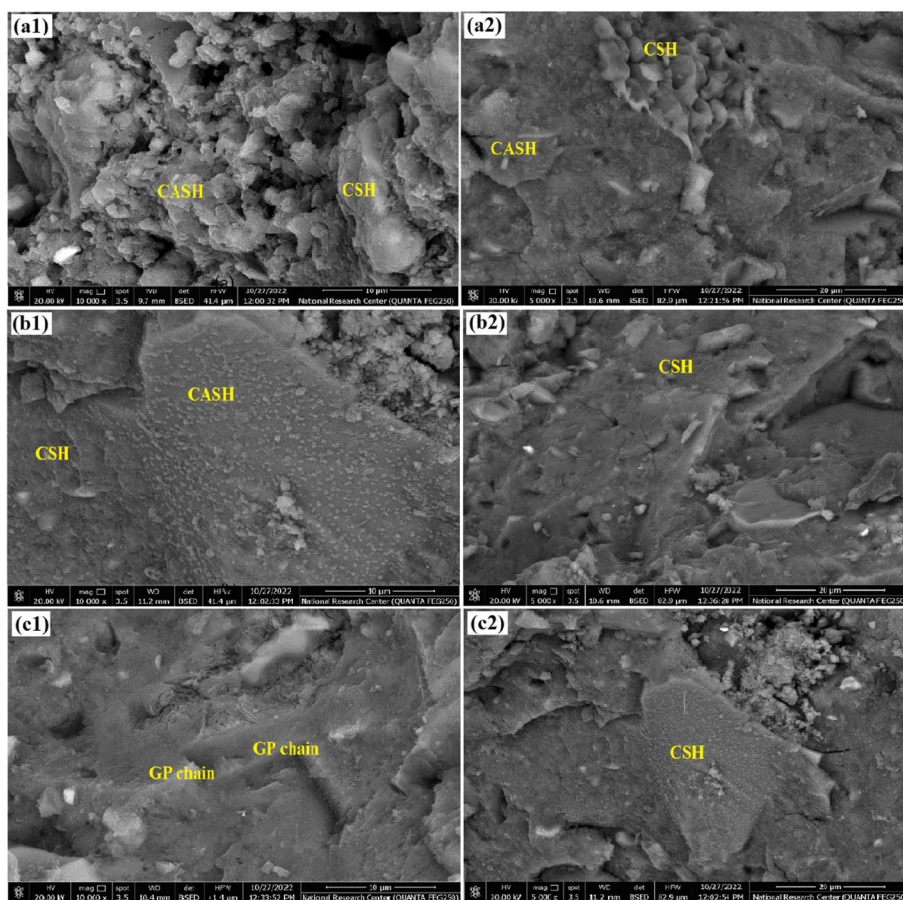
Fig. 14 SEM micrographs of mixes a1, a2 M, b1, b2 M20, and c1, c2 M20-T2 after 3 and 28 days of curing, respectively

photos clearly demonstrate that the geopolymer matrix is more compact, and that the quantity of CSH gels is increased, especially after 3 days of curing, demonstrating the beneficial effects of NT on GP structure (Fig. 15c1, c2) [66]. On the other hand, SEM micrographs of mixes M, M20, and M20-T2 after firing at 250 and 750 °C are shown in Fig. 15((a1, a2), (b1, b2), (c1, c2), respectively). After firing at 250 °C for 3 h, SEM pictures of mixes M, M2, and M20-T2 samples (Fig. 16a1, b1, and c1, respectively) reveal the production of larger quantities of CSH and CASH gel which surrounded the uncreated grains. These phases facilitate the improvement of the mechanical characteristics for these mixes. This observation agrees well with the mechanical features that have already been mentioned. Additionally, firing GP samples at 250 °C seemed to have an impact on the morphology of the produced hydrates as evidenced by the emergence of semi-crystals and short fibers of CSHs linking together inside the pores in mixes M and M20 or chain formation in mix M20-T2 micrographs. In micrographs of mixes M and M20 after firing at 750 °C (Fig. 16a2, b2, respectively), significant macropores and fractures are seen that have a deleterious impact on the mechanical characteristics [79]. On the other hand, mix M20-T2 exhibits minimal microcracks in SEM images at 750 °C, demonstrating the heat resistance of such composite (Fig. 15c2).
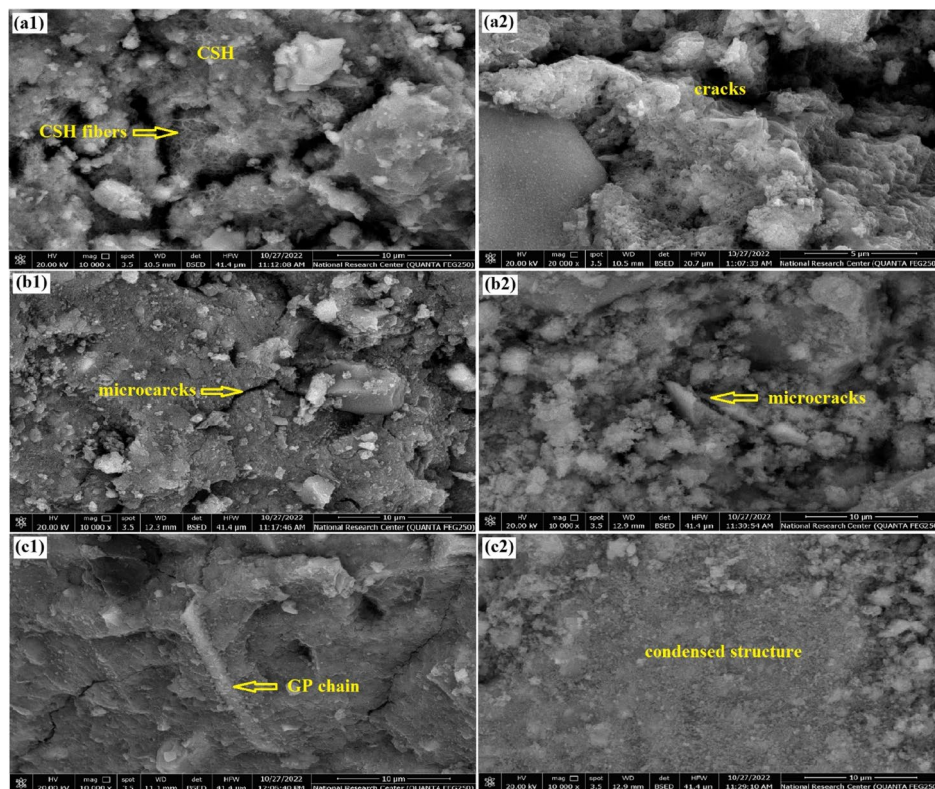
Mashout *et al. Journal of Engineering and Applied Science*   (2023) 70:106

Page 20 of 24

Fig. 15 SEM micrographs of mixes a1, a2 M, b1, b2 M20, and c1, c2 M20-T2 after firing at 250 and 750 °C, respectively

The impact of SO_4^{-2} ions on GP mixes due to their immersion in $MgSO_4$ solution is clearly noticeable in their SEM micrographs. SEM images of the M20-T2 composites reveal hexagonal plates of gypsum, whereas images of the M and M20 mixtures show ettringite (E) as crystalline needles [80] (Fig. 16).

Conclusions

The following conclusions may be drawn from our investigation's findings:

1. Blast furnace slag and basalt waste powders can be used to create one-part geopolymer cement with recognized mechanical properties and durability against distinct degradation processes.
2. The one-part geopolymer that was created had shorter setting times than OPC, but it nevertheless matched to ASTMC 150 M specifications.
3. Greater blending ratios (up to 60%) diminished the strength by around 30% after 28 and 90 days of curing, whereas substituting up to 20% of the slag with basalt powder improved the mechanical properties.
4. A geopolymer composed of 80% slag and 20% basalt exhibited resistance to gamma radiation, particularly at high doses (1000 and 1500 kGy). A suitable level of durability in MgSO4 solution and fire action up to 750 °C are also featured.
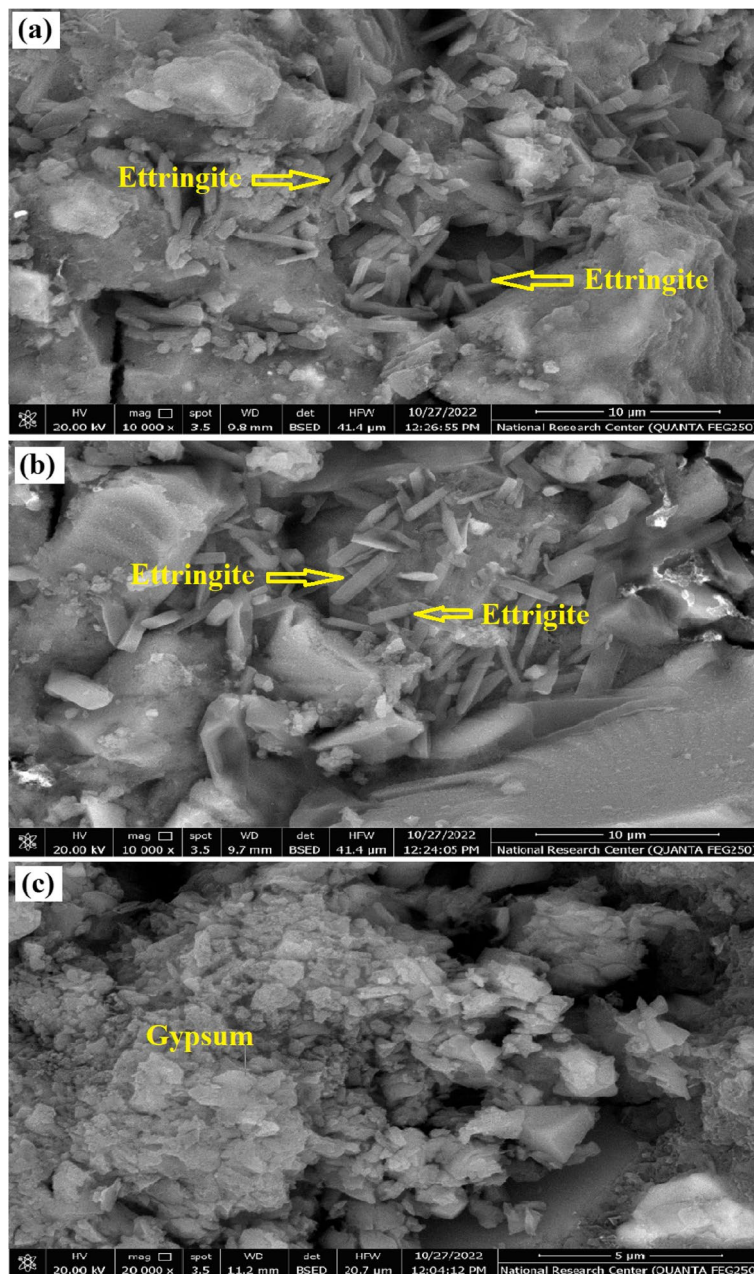
Fig. 16 SEM micrographs of mixes. **a** M, **b** M20, and **c** M20-T2 after immersion in MgSO$_4$ solution for 4 months

5. One-part slag/basalt-based geopolymer composite with 1% NT retains 100% and 65% of its strength when fired at 500 and 750 °C, respectively. In addition, this mixture is resistant to the effects of SO$_4{}^{-2}$ ions and large doses of gamma radiation. This is related to the catalytic action and filling properties of nano-TiO$_2$.

Abbreviations

NT	Nano-TiO_2
GP	Geopolymer composite
BW	Basalt waste
GGBFS	Ground granulated blast-furnace slag
CSH	Calcium silicate hydrates
CASH	Calcium aluminate-silicate hydrates
TG	Thermal gravimetric
PC	Portland cement
SEM	Scanning electron microscope
XRD	X-rays diffraction

Availability of data and materials
The data of this work can be shared upon request.

Declarations

Competing interests
The authors declare that they have no competing interests.

References
1. Schneider M, Romer M, Tschudin M, Bolio H (2011) Sustainable cement production—present and future. Cem Concr Res 41:642–650
2. Berndt MI (2009) Properties of sustainable concrete containing fly ash, slag and recycled concrete aggregate. Constr Build Mater 23:2606–2613
3. Josa A, Aguado A, Cardim A, Byars E (2007) Comparative analysis of the life cycle impact assessment of available cement inventories in the EU. Cem Concr Res 37(5):781–788
4. Kelly FJ, Fussell JC (2015) Air pollution and public health: emerging hazards and improved understanding of risk. Envir Geochem Heal 37(4):631–649
5. Flatt RJ, Roussel N, Cheeseman CR (2012) Concrete: an eco-material that needs to be improved. J Eur Ceram Soc 32:2787–2798
6. Gartner E, Hirao H (2015) A review of alternative approaches to the reduction of CO_2emissions associated with the manufacture of the binder phase in concrete. Cem Concr Res 78:126–142
7. Davidovits J (2013) Geopolymer cement, a review. Geopoly Inst Tech Pap 21(29):1–11
8. Turner LK, Collins FG (2013) Carbon dioxide equivalent (CO_2-e) emissions: a comparison between geopolymer and OPC cement concrete. Constr Build Mater 43:125–130
9. Abdel-Gawwad HA, Heikal EE, El-Didamony H, Hashem FS, Mohammed AH (2018) A new method to create one-part non-Portland cement powder. J Therm Analy Calor 134:75–52
10. Abdel-Gawwad HA, Heikal EE, El-Didamony H, Hashem FS, Mohammed AH (2018) Recycling of concrete waste to produce ready-mix alkali activated cement. Ceram Inter 44:7300–7304
11. Sultan ME, Abo-El-Enein SA, Sayed AZ (2018) EL-Sokkary TM, Hammad HA, Incorporation of cement bypass flue dust in fly ash and blast furnace slag-based geopolymer. C stud constr mater 8:315–322
12. Abo-El-Enein SA, Hashem FS, Amin MS, Sayed DA (2016) Physicochemical characteristics of cementitious building materials derived from industrial solid wastes. Constr Build Mater 126:983–990
13. Fadel O, Hehal EE, Hashem FS, Selim FA (2020) Mechanical properties, resistance to fire and durability for sulfate ions of alkali activated cement made from blast furnace slag- fine metakaolin. Egy J Chem 63:4821–4831
14. Robayo RA, Mulford A, Munera J, de Gutiérrez RM (2016) Alternative cements based on alkali-activated red clay brick waste. Constr Build Mater 128:163–169
15. Moraes I, Font A, Soriano L, Akasaki J, Tashima M, Monzó J, Borrachero M, Payá J (2018) New use of sugar cane straw ash in alkali activated materials: a silica source for the preparation of the alkaline activator. Constr Build Mater 171:611–621

16. Abdel-Gawwad HA, Heikal M, Mohammed MS, Abd El-Aleem S, Hassan HS, García SV, Alomayri T (2019) Sustainable disposal of cement kiln dust in the production of cementitious materials. J Cle Prod 232:1218–1229
17. Ebrahim NK, Ali A, Provis JL (2017) Calorimetric study of geopolymer binders based on natural pozzolan. J Therm Analy Calor 127:2181–2190
18. Bakharev T, Sanjayan JG, Cheng YB (2003) Resistance of alkali-activated slag concrete to acid attack. Cem Concr Res 33(10):1607–1611
19. Fertani-Gmati M, Jemal M (2015) Thermochemical and kinetic investigations of amorphous silica dissolution in NaOH solutions. J Therm Anal Calorim. https://doi.org/10.1007/s10973-015-4980-7
20. Kong DLY, Sanjayan JG (2010) Effect of elevated temperatures on geopolymer paste, mortar and concrete. Cem Concr Res 40:334–339
21. Singh NB, Middendorf B (2020) Geopolymers as an alternative to Portland cement: an overview. Constr Build Mater 237:117455
22. Lo KW, Lin KL, Cheng TW, Chang YM, Lan JY (2017) Effect of nano-SiO2 on the alkali-activated characteristics of spent catalyst metakaolin-based geopolymers. Constr Build Mater 143:455–463
23. Jindal BB (2017) Improving compressive strength of low calcium fly ash geopolymer concrete with alccofine. Adv Concr Constr 5(1):17–29
24. Luo HL, Lin DF, Chen SC (2017) Improving the properties of geopolymer containing oil-contaminated clay, metakaolin, and blast furnace slag by applying nano-SiO2. Environ Tech 38(13–14):1619–1628
25. Hassan A, Arif M, Shariq M (2019) Use of geopolymer concrete for cleaner and sustainable environment: a review of mechanical properties and microstructure. J Clean Prod 223:704–728
26. Alaa MR, Ahmed SO (2019) Thermal resistance of alkali-activated meta-kaolin pastes containing nano-silica particles. J Therm Analy Calor 136:609–620
27. Ye N, Yang J, Liang S, Hu Y, Hu J, Xiao B, Huang Q (2016) Synthesis and strength optimization of one-part geopolymer based on red mud. Constr Build Mater 111:317–325
28. Uysal M, Yilmaz K (2011) Effect of mineral admixtures on properties of selfcompactingconcrete. Cem Concr Comp 33:6–771
29. Constantiner D (2003) Diamond D, Alkali release from feldspar into pore solutions. Cem Concr Res 33:549–554
30. Hashem FS, Hekal EE, Abdel Naby MM, Selim FA (2021) Mechanical properties and durability performance against fire, gamma ray and bio-fouling of hardened Portland cement pastes incorporating lead bearing wastes. Mater Chem Phys 272:124–997
31. Sanad SA, Abel Moniem SM, Abdel-Latif ML, Hossei HA, El-Mahllawy MS (2021) Sustainable management of basalt in clay brick industry after its application in heavy metals removal. J Mater Res Technol 10:1493–1502
32. Dobiszewsk M (2017) Beyciõglu A, Investigating the influence of waste basalt powder on selected properties of cement paste and mortar. IOP Conf Ser Mater Sci Eng 245:22–27
33. El-Didamony M, Helmy IM, Osman RM, Habboud AH (2015) Basalt as pozzolana and filler in ordinary Portland cement. Am J Eng Appl Sci 8:263–274
34. Parveen S, Pham T (2020) Enhanced properties of high-silica rice husk ash-based geopolymerpaste by incorporating basalt fibers. Constr Build Mater 2020(245):118–422
35. Timakul P, Rattanaprasit W, Aungkavattana P (2016) Improving compressive strength of fly ash-based geopolymer composites by basalt fibers addition. Ceram Int 42(5):6288–6295
36. Li W, Xu J (2009) Mechanical properties of basalt fiber reinforced geopolymeric concrete under impact loading. Mater Sci Eng A 505(1):178–186
37. Garg M, Das CS, Gupta R (2020) Use of silica particles to improve dispersion of –COOH CNTs/carbon fibers to produce HyFRCC. Constr Build Mater 250:118–777
38. Massana J, Reyes E, Bernal J, León N, Sánchez-Espinosa E (2018) Influence of nano- and micro-silica additions on the durability of a high-performance self-compacting concrete. Constr Build Mater 165:93–103
39. Omid A, Masoud SN, Mostafa F, Mehdi M, Samira B (2015) Stable plasmonic-improved dye sensitized solar cells by silver nanoparticles between titanium dioxide layers. Electrochim Acta 152:101–107
40. Omid A, Masoud SN, Mostafa F (2015) Enhancement of dye-sensitized solar cells performance by core shell Ag@ organic (organic=2-nitroaniline, PVA, 4-choloroaniline and PVP): effects of shell type on photocurrent. Electrochim Acta 153:90–96
41. Araujoa FP, Honorioa LMC, Limaa IS, Trigueiroa P, Almeidab LC, Fechinec PBA, Santosa FEP, Peña-Garciaa R, Silva-Filhoa EC, Osajimaa JA (2020) New composite TiO2/naturals gums for high efficiency in photodiscoloration process. Ceram Int 46(10):15543
42. TS 25 (2008) Natural pazzolana (trass) for use in cement and concrete- definitions, requirements and conformity criteria. Turk Stand Instit Ankara.
43. Amin MS, El-Gamal SMA, Hashem FS (2015) Fire resistance and mechanical properties of carbon nanotubes – clay, bricks wastes (Homra) composites cement. Constr Build Mater 98:237–249
44. Nikoli V, Komljenovi M, Džunuzovi N, Miladinovi Z (2018) The influence of Pb addition on the properties of fly ash-based geopolymers. J Hazard Mater 350:98–107
45. ASTM C191 (2013) Standard test methods for time of setting of hydraulic cement by Vicat Needle
46. ASTM (2008) standard test method for compressive strength of hydraulic cement mortars. ASTM Inter, West Conshohocken, p 109
47. Kathirvel P, Kaliyaperumal M (2018) Performance of alkali activated slag concrete under aggressive environment. Sci Iran 25(5):2451–2460. https://doi.org/10.24200/SCI.2017.4221
48. Suwan T, Fan M (2017) Effect of manufacturing process on the mechanisms and mechanical properties of fly ash-based geopolymer in ambient curing temperature. Mater Manuf Process 32:461–467
49. ASTM C 150M (2012). Standard Specification for Portland cement
50. Madhu C (2021) Anjaneyulu, Malikarjuna M, Vara Prasad J, Impact of nano titanium dioxide on geopolymer concrete. Inter J Res Pub Rev 2(12):484–493

51. Hajimohammadi A, Provis JL (2011) van DeventerJSJ, Time-resolved and spatially resolved infrared spectroscopic observation of seeded nucleation controlling geopolymer gel formation. J Colloid Inter Sci 357:384–392
52. Liu Y, Zhu W, Yang EH (2016) Alkali-activated ground granulated blast-furnace slag incorporating incinerator fly ash as a potential binder. Constr Build Mater 112:1005–1012
53. Castillo H, Collado H, Droguett T, Sánchez S, Vesely M, Garrido P (2021) Factors affecting the compressive strength of geopolymers: a review. Minerals 11(12):1317
54. Ismail I, Bernal SA, Provis JL, San Nicolas R, Hamdan S, van Deventer JS (2014) Modification of phase evolution in alkali-activated blast furnace slag by the incorporation of fly ash. Cem Concr Comp 45:125–135
55. Zawrah M, Gado R, Khattab R (2018) Optimization of slag content and properties improvement of metakaolin-slag geopolymer mixes. Open Mater Sci J 12(1) 40–57
56. Shchelokova EA, Tyukavkina VV, Tsyryatyeva AV, Kasikov AG (2021) Synthesis and characterization of SiO2-TiO2 nanoparticles and their effect on the strength of self-cleaning cement composites. Constr Build Mater 283:12
57. Provis JL, Myers RJ, White CE, Rose V, Van Deventer JS (2012) X-ray microtomography shows pore structure and tortuosity in alkali-activated binders. Cem Concr Res 42(6):855–864
58. El-Gamal SMA, Hashem FS, Amin MS (2017) Influence of carbon nanotubes, nanosilica and nanometakaolin on some morphological-mechanical properties of oil well cement pastes subjected to elevated water curing temperature and regular room air curing temperature. Constr Build Mater 146:531–546
59. Zawrah M, Rabei S, Kohail MH (2018) Improvement of physical and mechanical properties of geopolymer through addition of zircon. Mater Chem Phys 217:6–24
60. Rashad AM, Sadek DM, Hassan HA (2016) An investigation on blastfurnace stag as fine aggregate in alkali-activated slag mortars subjected to elevated temperatures. J Clean Prod 112:1086–1096
61. Duan P, Yan C, Luo W, Zhou W (2016) Effects of adding nano-TiO2 on compressive strength, drying shrinkage, carbonation and microstructure of fluidized bed fly ash based geopolymer paste. Constr Build Mater 106:115–125
62. Jagadesh P, Nagarajan V, Karthikprabhu T, Arunachalam KK (2022) Effect of nano titanium di oxide on mechanical properties of fly ash and ground granulated blast furnace slag based geopolymer concrete. J Build Eng 61:105–235
63. Hashem FS (2009) Sulfate attack on hardened cement pastes with different porosities in the presence of water-repelling admixtures. Adv Cem Res 21:75–82
64. Selim FA, Hashem FS, Amin MS (2020) Mechanical, micro-structural and acid resistance aspects of improved hardened Portland cement pastes incorporating marble dust and fine kaolinite sand. Constr Build Mater 251:118–992
65. Parthiban K, Mohan KSR (2017) Influence of recycled concrete aggregates on the engineering and durability properties of alkali activated slag concrete. Constr Build Mater 133:65–72
66. Chen J, Kou S, Poon C (2012) Hydration and properties of nano TiO2 blended cement composites. Cem Concr Comp 34:642–649
67. Öztürk BC, Kızıltepe CC, Ozden B, Güler E, Aydın S (2020) Gamma and neutron attenuation properties of alkali-activated cement mortars. Radiat Phys Chem 166:108478
68. El-Faramawy N, Ramadan W, El-Zakla T, Sayed M, El-Dessouky M, Sakr K (2015) Effect of ilmenite on the attenuation coefficient of gamma ray shielding cementious matrix. Radiat Eff Defects Solids 170(11):876–886
69. Al-Hamarneh IF (2017) Investigation of gamma-ray shielding effectiveness of natural marble used for external wall cladding of buildings in Riyadh Saudi Arabia. Results Phys 7:1792–1798
70. Lambertin D, Boher C, Dannoux-Papin A, Galliez K, Rooses A, Frizon F (2013) Influence of gamma ray irradiation on metakaolin based sodium geopolymer. J Nucl Mater 443(1–3):311–315
71. Yip CK, Lukey GC, van Deventer JSJ (2005) The coexistence of geopolymeric gel and calcium silicate hydrate at the early stage of alkaline activation. Cement Concr Res 35:1688–1697
72. Christina K, Yip Grant C, Lukey John L (2008) Effect of calcium silicate sources on geopolymerisation. Cem Concr Res 38:554–564
73. Bernal SA, Provis JL, Rose V, de Gutierrez RM (2011) Evolution of binder structure in sodium silicate-activated slag-metakaolin blends. Cem Concr Compos 33(1):46–54
74. Türker HT, Balçikanli M, Durmuş IH, Özbay E, Erdemir M (2016) Microstructural alteration of alkali activated slag mortars depend on exposed high temperature level. Const Build Mater 104:169–180
75. Lee BY, Jayapalan AR, Kurtis KE (2013) Effects of nano TiO$_2$ on properties of cement-based materials. Mag Concr Res 65:1293–1302. https://doi.org/10.1680/macr.13.00131
76. Nazari A, Riahi S (2011) TiO$_2$ nanoparticles effects on properties of concrete using ground granulated blast furnace slag as binder. Sci China Technol Sci 54(11):3109–3118. https://doi.org/10.1007/s11431-011-4421-1
77. Ma B, Li HH, Mei J, Li X, Chen F (2015) Effects of TiO2 on the toughness and durability of cement-based materials. Adv Mater Sci Eng 1–10. https://doi.org/10.1155/2015/583106.
78. Zhang Y, Chang J, Ji J (2018) AH3 phase in the hydration product system of AFt-AFm-AH3 in calcium sulfoaluminate cements: a microstructural study. Constr Build Mater 167:587–596. https://doi.org/10.1016/j.conbuildmat.2018.02.052
79. El-Gamal SMA, Hashem FS (2017) Enhancing the thermal resistance and mechanical properties of hardened Portland cement pastes by using pumice and Al$_2$O$_3$. J Therm Anal Calor 128:15–27
80. Ali AZM, Sanjayan J, Guerrieri M (2017) Performance of geopolymer high strength concrete wall panels and cylinders when exposed to a hydrocarbon fire. Construct Build Mater 137:195–207. https://doi.org/10.1016/j.conbuildmat.2017.01.099

Publisher's Note